



JOURNAL OF THE INTERNATIONAL SOCIETY FOR RESPIRATORY PROTECTION

**A Mobile App to Measure Facial
Dimensions and Predict Respirator
Size**

1

*Eric Elliott, Medhat Korna, Gregory Van Ermen, Daniel Barker, and
John Lloyd*

**The Effect of Particle Size, Membrane
Type, and Face Velocity on TiO₂-
Containing Paint Dust Filtration**

16

*Adam W. Nored, Marie-Cecile G. Chalbot, Jin Y.
Shin and Ilias G. Kavouras*

ISRP Oxford Conference 2024

26

Instructions for Authors

27

JISRP

Editor in Chief

Ziqing Zhuang, Ph.D.

National Personal Protective Technology Laboratory
National Institute for Occupational Safety and Health
Pittsburgh, PA (USA)
JISRPeditor@ISRP.com

Editorial Review Board

David Caretti, M.S.
U.S. Army Edgewood Chemical Biological Center (USA)

Eva Dickson, Ph.D.
Defence R&D Canada and the Royal Military College of Canada (Canada)

Xinjian He, Ph.D.
China University of Mining and Technology (China)

Jung-Hyun (Kenny) Kim, Ph.D.
Kyung Hee University (South Korea)

Youcheng Liu, Sc.D.
Wayne State University (USA)

Toshihiko Myojo, Ph.D.
University of Occupational & Environmental Health (Japan)

Richard W. Metzler, M.S.
Richard W. Metzler, Inc. (USA)

Michael Parham, M.S., P.E.
3M Company (USA)

Margaret Sietsema, Ph.D.
University of Illinois at Chicago (USA)

Leo Steenweg, Bsc
Consultant (Netherlands)

Meghan Swanson, Ph.D.
MSA Company (USA)

Mike Williams, Ph.D.
Cranfield University (UK)

International Society for Respiratory Protection

Officers and Board of Directors
2020-2022

Officers

PRESIDENT

Eva Dickson
Defence R&D Canada and
the Royal Military
College of Canada

SECRETARY

Jessica Hauge
3M Company

VICE PRESIDENT

Gabriele Troescher
3M Company

TREASURER

Jessica Hauge
3M Company

PAST PRESIDENT

Michael Parham
3M Company

Members of the Board

Americas Section:

Jonathan Szalajda
John Morris
Greg Olson
Margaret Sietsema

European Section:

David Crouch
Mike Lee
Karen Long
Mike Williams

Greater Chinese Section:

Weihong Chen
Zhongxu Wang

Australasian Section:

Graham Powe
Straff Graso

Japan Section:

Toshihiko Myojo
Isao Kuniya
Hiroshi Yamada
Hisashi Yuasa

Korea Section:

Don-Hee Han
Seong-Kyu Kang
Deog-jae Lee
Jung-Keun Park



The Journal of the International Society for Respiratory Protection (*JISRP*), ISSN 0892-6298, is a copyrighted publication of the International Society for Respiratory Protection (ISRP), 1504 Asbury St. N, Saint Paul, MN 55108 USA, <http://www.isrp.com/>. No part may be reprinted without express written consent of the ISRP.

The JISRP is a forum for open and responsible discussion in the field of respiratory protection. All opinions published herein are solely those of the authors.

The ISRP is a non-profit organization whose charter is to provide an educational and informational service to all individuals involved in respiratory protection. The JISRP is published semiannually and provided free of charge to ISRP members in good standing. Instructions for submitting manuscripts, articles and letters can be found at the back of this publication.

This Journal was edited by Ziqing Zhuang, Ph. D., 105 Eaglebrook Court, Venetia, PA 15367 USA, tel: +1-412-848-0409, JISRPEDITOR@ISRP.COM; in his private capacity. No official support or endorsement by CDC is intended or should be inferred.

For general information regarding membership, journal subscriptions, etc, visit www.ISRP.com or contact any of the Section representatives named below:

The Americas
Heidi Sewchok
vmu2@cdc.gov

Australasia
Sophie Foot
Sophie.foot@sea.com.au

Greater China
Weihong Chen
wchen@tjmu.edu.cn

Europe
Mike Williams
secretary@isrpeurope.com

Japan
Toshihiko Myojo
tmyojo@med.uoeh-u.ac.jp

Korea
Won-Souk Eoh
ahardworker@hanmail.net

Journal of the International Society for Respiratory Protection

Vol. 38, No. 1, 2021

- 1 A Mobile App to Measure Facial Dimensions and Predict Respirator Size ... *Eric Elliott, Medhat Korna, Gregory Van Ermen, Daniel Barker, and John Lloyd*
- 16 The Effect of Particle Size, Membrane Type, and Face Velocity on TiO₂-Containing Paint Dust Filtration ... *Adam W. Nored, Marie-Cecile G. Chalbot, Jin Y. Shin and Ilias G. Kavouras*
- 26 ISRP Oxford Conference 2024
- 27 Instructions for Authors



Letter from the ISRP President

Dear Members,

Given that we have all been in various stages of lockdown and reopening since my last letter, the Society has been focussed primarily on activities that can be delivered on-line. The Journal of the ISRP continues its smooth transition to fully on-line delivery, and the Journal Improvement committee has been negotiating the indexing of the journal for the first time. The European section continues to deliver a very successful webinar series (<https://www.isrp.com/2021-european-workshop-programme>). Finally, the executive has been laying the groundwork for the 2022 International Society conference, to be held virtually, with the majority of the conference committee now recruited and ready to start work organizing the conference, including engaging the platform and developing the technical program. We hope this



will be an opportunity to reach our members world-wide in a forum accessible to all, and we encourage anyone with questions or who would like to help to contact me, as Conference Chair, at president@isrp.com. The Oxford International Society conference is now firmly scheduled for September 22nd to 26th 2024 and we hope to see you all there, but in the meantime, we will take this opportunity to re-engage in the new ways we have found.

In disappointing news, the UK government has withdrawn significant committed research and innovation funding in the area of overseas development, which includes the FACE-UP project on protection of children from urban particulates in which we were a partner. There has been a groundswell of support to reinstate the full funding, and we have signed an open letter calling on the UK government to reverse the cuts, as discussed here <https://www.bbc.com/news/science-environment-56460154>.

Finally, I hope you have an opportunity to relax a bit more where COVID-19 numbers are starting to drop, and where they are not yet, know that we all support you in your quest to protect everyone in the best manner possible. Please continue to do the good work you have been doing, supporting new protection standards and delivering world-class advice and protective equipment to those who need it.

Sincerely,

Eva Dickson
President, ISRP

president@isrp.com

Defence Research & Development Canada and Royal Military College of Canada

A Mobile App to Measure Facial Dimensions and Predict Respirator Size

Eric Elliott^{1*}, Medhat Korna¹, Gregory Van Ermen¹, Daniel Barker², and John Lloyd²

¹ Technology Solutions Experts, Inc., 209 West Central Street, Suite 202, Natick, MA 01760, USA, USA

² Edgewood Chemical Biological Center, Research and Technology Directorate, ATTN: RDCB-DRP-R, Bldg. 3400, Aberdeen Proving Ground, MD 21010-5424, USA

* Corresponding author and E-mail: eric.elliott@tseboston.com

ABSTRACT

The current workflow for sizing military respirators is time consuming, manually intensive, and tedious, but is necessary due to the critical need for respirators to fit properly, especially in operating environments when Warfighters may be exposed to chemical, biological, radiological, and nuclear threats. To reduce the time and resource cost of the fitting process, Technology Solutions Experts, Inc. developed a software application to rapidly generate a 3D model of a user's face, accurately compute anthropometric measurements, and estimate the appropriate size of a respiratory protective mask. In this paper, we discuss implementing our 3D model generation and size prediction methodology in a mobile app, and collecting and analyzing data to measure the methodology's predictive capability. Our verification and validation results show that our current method for fit prediction is insufficient to replace traditional fit tests. However, there is evidence to suggest that face measurements obtained from 3D models can produce fit predictions as accurate as hand measurements but in a fraction of the time, and without subject matter expertise.

Keywords: Respirator, mask, fit, 3D, model, prediction, face, images, measurements, anthropometry

INTRODUCTION

Military respirators are critical to the survival of Soldiers who are exposed to chemical, biological, radiological and nuclear (CBRN) threats. The fit of the respirator on the wearer directly determines whether the respirator will effectively protect against foreign agents. Identifying the correct size of a full facepiece respirator for an individual requires specialized equipment for measuring aerosols within the mask, an operator trained to use the fit testing equipment and interpret its results, and the time and colocation of both operator and testing subject. The Chemical and Biological Defense (CBD) program seeks a quicker, less manually intensive, yet reliable method to select the correct respirators for individuals and to approximate the fit factor.

Through a Small Business Innovative Research (SBIR) grant, Technology Solutions Experts Inc. (TSE) developed a method to generate 3D head forms (3DHF) from 2D images, estimate facial measurements, and to predict the appropriate size of the Avon C50 respirator for an individual using the estimated measurements. To deploy this methodology and make it available to a wide audience, we

developed MASQ (Mask Analysis and Size Quantification), a mobile app capable of running on common Android and iOS phones (shown in Figure 1). In this paper we present the results of our research and development, and an analysis of the predictive capabilities of the methodologies we developed for MASQ.

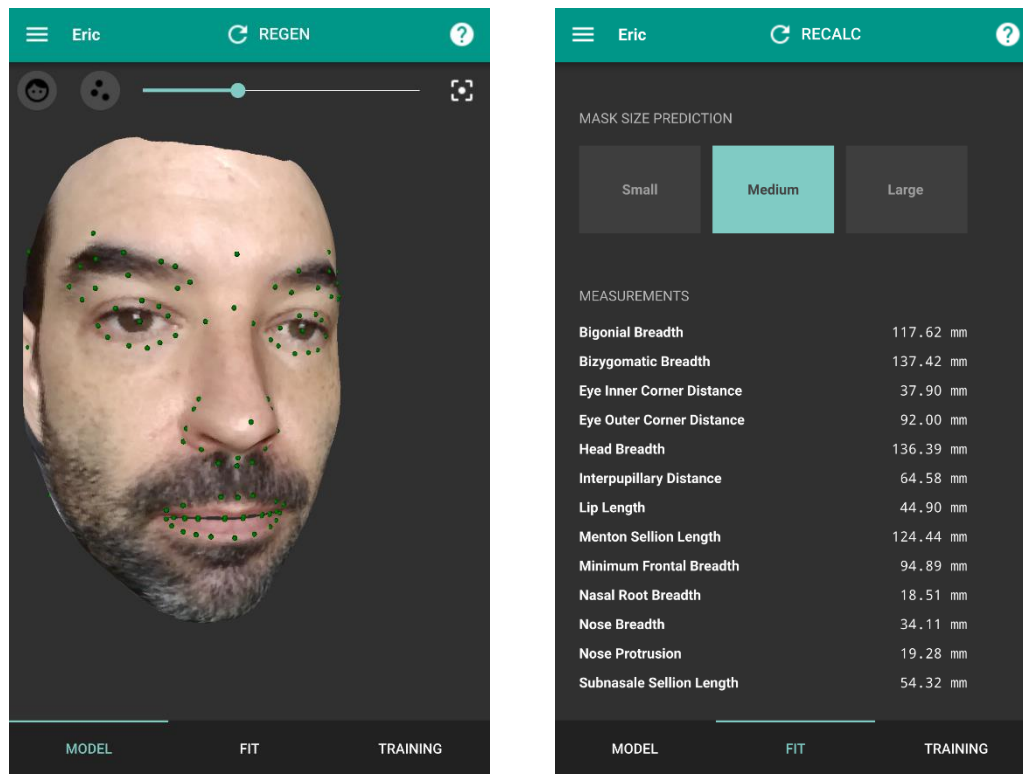


Figure 1. Screenshots of MASQ showing a generated 3D model (left), and estimated facial measurements (right).

Summary of Previous Work

We previously researched and developed a method to generate 3DHF from 2D images and implemented a proof of concept application to demonstrate the feasibility of the approach. This work is detailed in a previous paper (Biagiotti, Korna, Rice, & Barker, 2019) and summarized here for background and context.

To generate 3D models, MASQ first detects a set of 68 facial landmarks on input images (shown in Figure 2) and then uses the landmarks to transform vertices on a base 3D model into a final 3D representation of the input images. MASQ uses a 3rd party open source C++ library called eos (Huber P. , A lightweight 3D Morphable Face Model fitting library in modern C++, 2016) to both estimate the locations of facial landmarks and to morph the corresponding vertices on the base model.

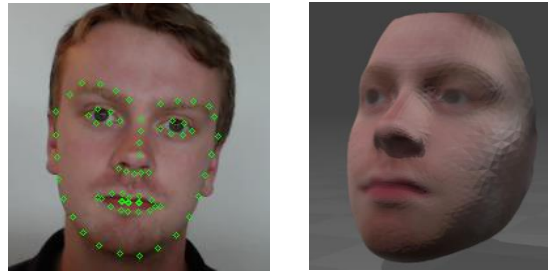


Figure 2. Example of landmark detection (left) and resulting 3D head form (right).

The eos library utilizes the Surrey Face Model (SFM), a 3D face model parameterized via principle component analysis (PCA) to identify the dimensions of highest variation. The SFM was constructed from a set of 169 head scans encompassing a broad set of demographics, though not necessarily representative of the U.S. military population. Table I lists the age and racial and breakdown of the subjects that were used to construct the SFM.

Table I. Demographics of Subjects Used to Construct the SFM

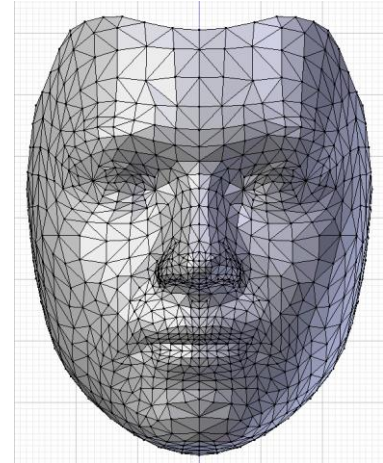
Age Group (years)	# of Subjects
0-19	9
20-29	106
30-44	33
45-59	13
60+	8
Perceived Race	# of Subjects
Caucasian	101
Black	10
Eastern Asian	34
South Asian, Arabic, or Latin American	24

For each set of input landmarks, MASQ estimates the pose angle of the face to properly orient the input landmarks, maps the 2D landmarks to their 3D counterparts on the base model, and extracts a texture from the source image to overlay on the final 3D model. Figure 2 shows an example of the final textured 3D head form constructed from the 2D image input.

MATERIALS AND METHODS

Our proof of concept relied on several manual steps, including identifying anthropometric landmarks (ALs) on generated 3DHF, and converting facial dimensions from dimensionless model units to mm by measuring test subjects. To transition to a mobile device workflow we developed methods to automatically identify landmarks on 3D models and to compute measurements in mm without hand-measurements. We then implemented methods for improving accuracy of generated 3DHF and finally performed a verification and validation (V&V) study to measure the performance of MASQ's facial measurement estimation and size prediction algorithms.

In our proof of concept we used the Maya 3D authoring application to manually identify points on generated 3DHF that corresponded to ALs of interest, and to compute linear distances between two landmarks to get facial dimension measurements. The landmarks that are used for face detection and 3D model generation are commonly used for face detection (Sagonas, Tzimiropoulos, Zafeiriou, & Pantic, 2013), but they don't necessarily correspond to the landmarks we use for facial measurement, so we needed a method to automate landmark identification and dimension measurement. We explored analyzing the structure of a generated model to identify regions and landmarks. For example, one could analyze the 3D triangle mesh to identify structures like eyes and lips, then locate the extents of the structures to identify eye and lip corners (Figure 3). However, many landmarks have more nuanced criteria for identification, which we determined would have led to unreliable placements.



Mask Filter

Model Viewer

68 facial landmarks (IDs):

- shape[286]
- shape[282]
- mouth[253]
- pronase[114]
- subnasale[90]
- left_gonion[160]
- right_gonion[169]
- left_ear[64]
- right_ear[71]
- left_nasale_root[62]
- right_nasale_root[199]
- left_alare[226]
- right_alare[242]
- left_head_exter[185]
- right_head_exter[185]
- left_foretemp[110]
- right_foretemp[208]
- left_eyegon[70]
- right_eyegon[77]
- left_chellon[61]
- right_chellon[38]

bilateral_breadth

real: 0
model: 124.0242388916016
scaled: 0
% error: NaN

biometric_breadth

real: 0
model: 134.132803466797
scaled: 0
% error: NaN

head_breadth

real: 0
model: 139.40687561035156
scaled: 0
% error: NaN

interpupillary_distance

Instead, we used the fact that the number and ordering of vertices in a generated model are the same as the base morphable model, only differing in their absolute positions. To make use of this, we manually identified the vertices on the base morphable model that corresponded to our landmarks of interest. This was a one-time process done via visual inspection to produce a mapping of vertex number to landmark. With this mapping, MASQ is able to find the vertex, and therefore the coordinates, of each landmark on a generated model automatically via a simple lookup (Figure 4).

The 3DHF that MASQ generates are dimensionless, so without additional information, there is no way to compute measurements in mm which is required for predicting mask size. To transform the 3DHF into mm, we first estimate a measurement in mm between two landmarks on a 2D image of the subject. We then use that distance and the corresponding distance in 3D model units to compute a ratio which is then used to scale the 3D model into mm.

Determining distances between landmarks in images requires either knowledge of photo parameters including the lens focal length, distance from lens to subject, and camera sensor size, or identifying an object in the image that has a known size. Because determining distance from lens to subject is difficult and imprecise, we developed a method for detecting an object of known dimension (OKD) in the image and using it to calculate the size in millimeters (mm) of a single pixel in the image by counting the width in pixels of the known object.

$$MMPerPixel = \frac{KnownObjectWidth_{mm}}{KnownObjectWidth_{px}}$$

Given a pixel size, we can then compute a distance in mm between any two points in the image. We use MASQ's landmark detection capabilities to identify the outer corners of the eyes and compute the eye outer corner (EOC) distance as the number of pixels from corner to corner, multiplied by the pixel size to get the distance in mm. While any facial dimension could be used as the reference measurement, the OKD should be located along the same linear path as the reference dimension in order to maximize accuracy. Holding an object to the eye corners achieves that goal while also being easy for the user to understand and accomplish.

$$EOC_{mm} = EOC_{px} * MMPerPixel$$

We then use the EOC distance in mm and the EOC distance in 3DHF units to derive the number of mm per 3DHF unit, thus allowing us to convert any measurement in 3DHF unit into mm.

$$MMPer3DHF = \frac{EOC_{mm}}{EOC_{3DHF}}$$

Known Object Detection and Measurement

Any object can be used for the purposes of this method, as long as its dimensions are known and consistent and it is placed on the same plane as the outer corners of the eyes. After evaluating numerous options, we selected the credit card as the OKD for initial implementation and subsequently added an additional option for using a custom shape, which produces results that are more reliable.

Credit Card Scaling

Most banking and ID cards conform to the ISO/IEC 7810 ID-1 standard (53.98mm x 85.60mm). Our approach combines Canny edge detection (Canny, 1986), Hough line detection (Matas, Galambos, & Kittler, 2000), and a ranking algorithm to identify the top and bottom lines of a credit card in an image, as seen in Figure 5. The distance between these lines is then measured in pixels. The real height of the card (53.98mm) is divided by the distance producing the mm/pixel ratio.

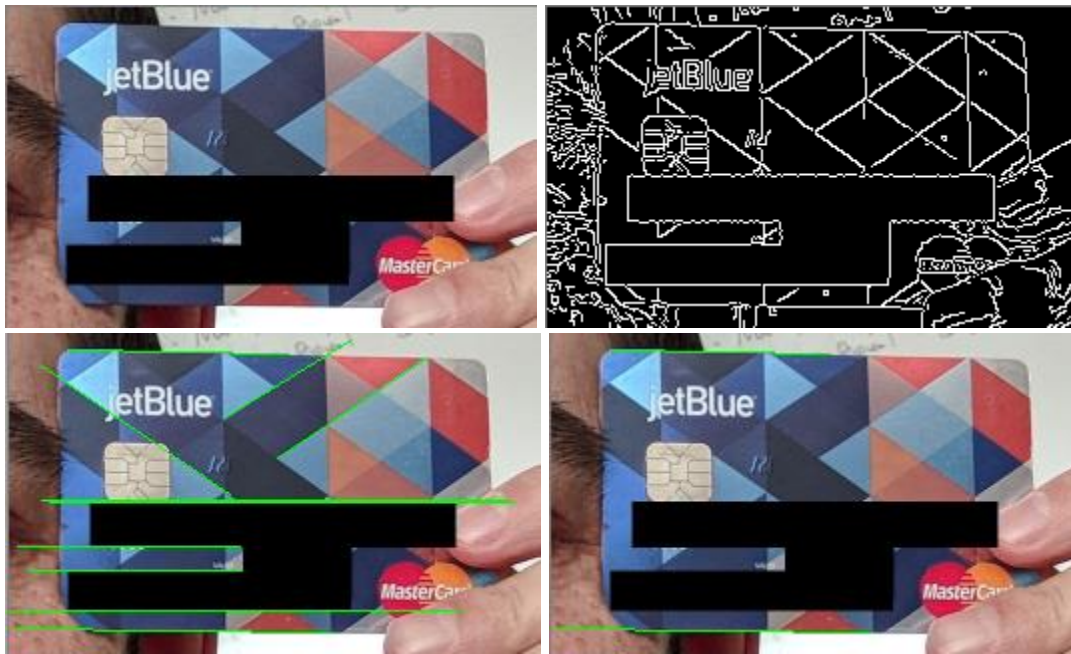


Figure 5. Scale calculation image processing from original image (top left), to Canny edge detection (top right), to Hough line detection (bottom left), and the final top and bottom lines by rank (bottom right).

Custom Scale Card

We found that identifying a credit card with potentially different colors and markings could be unreliable. Consequently, we experimented with using different shapes that can be more easily detectable. The downside of using a custom shape is that a user must print out the shape, but the improved detection reliability is substantial. Figure 6 shows a scaling image printed out on a business card and held next to the eyes just as with a credit card.

Using this shape allows us to use a simplified detection method that first translates the image to black and white, and then finds a continuous region of black pixels that matches the known height/width ratio of the black rectangle on the predefined image. Instead of using edge detection to find the extents of the black square, MASQ uses the contour detection functions provided by OpenCV to find all of the curves that are continuous, non-overlapping sets of pixels of the same color. Once detected, curves that don't have bounding rectangles matching the ratio of the scaling card, and those that are too small a percentage of the overall image are excluded. The remaining contour is then shown to the user to confirm detection was successful. While we didn't perform rigorous automated testing, we manually tested both credit card and scaling card detection in many different lighting and background conditions. From this it was clear that the scaling card resulted in far fewer failed or incorrect detections, faster detections, and better accuracy.



Figure 6. Scaling card held next to eyes to provide reference scale.

Improving Model Accuracy

In an effort to improve the accuracy of generated 3D models, we explored the benefits of using a higher resolution morphable model, increasing the number of landmarks detected per 2D image, and modifying various parameters in the 3D generation process to identify optimal settings.

Model Resolution

In our proof of concept, we used the lowest resolution of the Surrey Face Model, consisting of 7448 vertices, as the basis for generating 3DHF. We later acquired the high (29587 vertices) resolution model in order to test the benefits of increased vertex density on model generation accuracy. Figure 7 shows wireframe models of three resolutions of the SFM.

Although offering the potential for improved accuracy, additional vertices also lead to the potential for increased error. We found that the high-resolution model provided no benefit to model accuracy as any benefit of increased resolution was offset by any inaccuracies being equally magnified. The high-resolution model also resulted in a substantial increase in processing time, and as a result we chose to use the low-resolution model until new methods are developed to improve 2D landmark and pose detection. We anticipate that combining the high resolution model with perfectly accurate 2D landmark detection would improve overall accuracy but we have not tested that hypothesis.

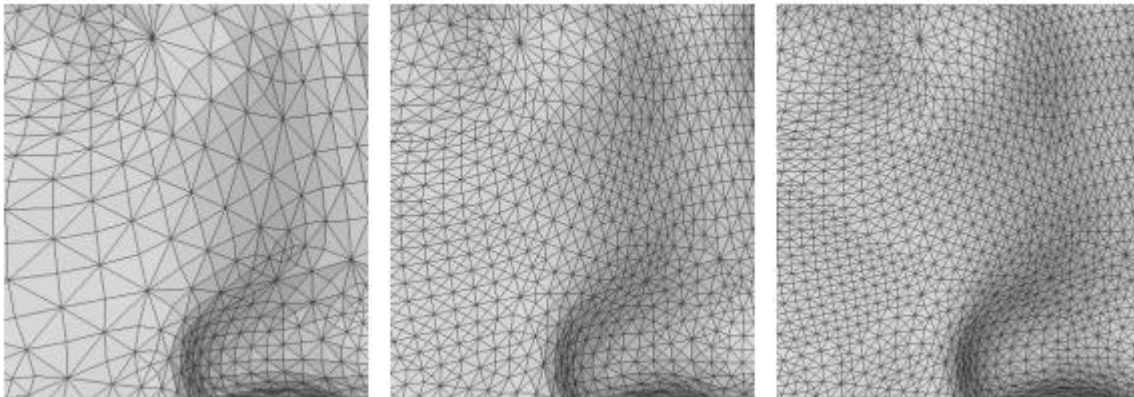


Figure 7. Morphable model resolutions (from left to right): 3448 vertices, 16758 vertices, 29587 vertices.

Landmark Density

Another method to improve model generation accuracy is to detect and map more points on the input images. To increase the number of landmarks used for transforming the morphable model, we trained a new landmark detection model using 103 landmarks instead of the original 68. To train and test the new detection model, we obtained the Helen dataset (Le, 2017), which consists of face images from the photo sharing website Flickr, annotated with landmarks to locate the eyes, nose, mouth, eyebrows, and jawline. An example of the detected landmarks is shown in Figure 8. When compared with landmarks from Figure 2, additional landmarks around the brows and nose can be observed, as well additional landmark density in the lips, eyes, and jawline.

We updated MASQ to support configuration of the landmark detection model in order to facilitate testing with both the original 68-landmark model and the 103-landmark model. As with increasing the morphable model resolution, the added landmark density also introduces potential for new errors. Since 3D model accuracy is dependent on the accuracy of 2D landmark detection and location, the increased

number of landmarks means there is more opportunity to introduce errors. While we didn't measure the accuracy of 2D landmark detection using 68 and 103 landmarks independently, we did test the final 3D headform accuracy when using each option. The landmark detection model is just one of many configurable options that we tested, with results for various configurations shown in section 4.

Parameter Configuration

In addition to model resolution and landmark density, we explored how the number and pose angle of images used to generate the model impacted model accuracy. The model can utilize multiple images of the same subject to refine the PCA parameters that define the final 3D headform. More images can both improve or degrade accuracy, largely dependent on how accurately landmarks are located on the 2D images. As the angle between the camera and the subjects facing direction, which we refer to as the pose angle, deviates from 0 degrees (facing the camera) to -90 degrees or 90 degrees (left or right profile), accuracy of landmark location tends to decrease. To filter out images that may result in inaccurate landmarks, we specify a configurable maximum pose angle (MPA). However, the pose angle is computed based on the detected landmarks, so filtering out potentially inaccurate landmarks is dependent on a measurement derived from those same landmarks. While not ideal, at worst it will include some images that should have been excluded, as opposed to excluding good images. To explore what parameters produced the best results, we tested a variety configurations of model resolution, landmark density, image count, and maximum pose angle. The results of these experiments are shown in section 4.

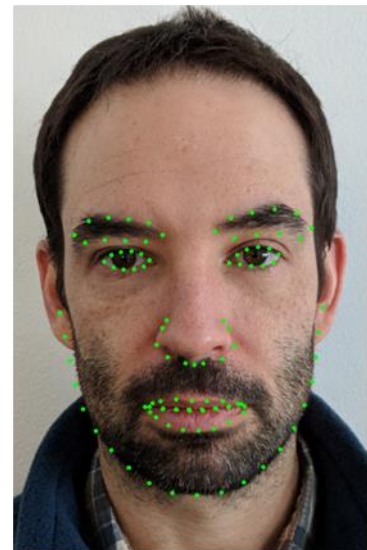


Figure 7. Subject annotated with 103 detected landmarks.

Verification and Validation

To verify and validate the algorithms used by the MASQ app, we employed an independent expert in anthropometry and fit testing to collect data on a set of subjects. For each subject, fit tests were administered for the Avon C50 respirator, anthropometric dimensions were hand-measured, and photos and videos were taken. Using these data, we measured the accuracy of 2D image scale estimates, facial dimension estimates, and mask size predictions produced by the MASQ algorithms.

Data Collection Protocol

To select subjects and perform data collection, we employed Anthrotech Inc., (<https://anthrotech.net/>), an independent company with expertise in anthropometry and fit testing. Anthrotech collected data for 36 subjects, with facial measurements distributed across a previously developed fit panel (Zhuang, Bradtmiller, & Shaffer, New Respirator Fit Test Panels Representing the Current U.S. Civilian Workforce, 2007).

Subjects were measured using procedures outlined in the *Measurer's Handbook: U.S. Army Anthropometric Survey* (Clauser, Tebbetts, Bradtmiller, McConville, & Gordan, 1987-1988), by one of two experts with extensive knowledge and background in identifying landmarks and measuring the identified dimensions. Each dimension was measured once using common measurement equipment, including sliding and spreading calipers, while the subject was either standing or sitting.

For each subject, five different types of data were recorded:

1. Facial measurements for 12 facial dimensions: Bigonial Breadth, Bizygomatic Breadth, Eye Outer Corner Distance, Head Breadth, Interpupillary Distance, Lip Length, Menton-Sellion Length, Minimum Frontal Breadth, Nasal Root Breadth, Nose Breadth, Nose Protrusion, Subnasale-Sellion Length
2. A forward facing image of the subject with a 2D scaling card held to the side of their face
3. A ~10 second video of the subject's head as they rotated from one side to the other
4. A fit test score produced by following the OSHA standard fit test protocol (OSHA Standards) for up to 3 different sizes (S, M, L) of the Avon C50 respirator
5. Basic demographic data including sex, age, height, weight.
 - a. This data was not used in this study, we collected in case it may prove useful in future research to refine the model.

2D Image Scale Estimation

For each of the 36 subjects, we used MASQ to estimate the eye outer corner (EOC) distance based on an image of the subject holding a scaling card, as described in section 3.2. We then computed the error of the estimation as:

$$EOC_{err} = \frac{|EOC_{est} - EOC_{real}|}{EOC_{real}}$$

Where,

EOC_{err} : Eye Outer Corner distance error

EOC_{real} : Measured distance in mm between eye outer corners

EOC_{est} : Estimated distance in mm between eye outer corners computed from scaling card

Facial Dimension Estimation

To compute facial dimension measurements, we used MASQ to generate a 3D model of the subject's head from a set of 2D images extracted from the video of the subject rotating their head from side to side. The generated 3D model is made up of dimensionless vertices, and each measurement is a dimensionless distance between two 3D points. To convert to millimeters, we used the estimated EOC distance discussed in section 3.4.2 to derive a scaling factor as described in section 3.2. For each subject, we applied the scaling factor to compute a measurement in mm for each of the 12 dimensions, and then computed the measurement error for each dimension as:

$$M_{err} = \frac{|M_{est} - M_{real}|}{M_{real}}$$

Where,

M_{err} : Estimated measurement error

M_{est} : Estimated measurement

M_{real} : Real measurement

We then computed the average error across all dimensions for each subject, the average error across all subjects for each dimension, and an aggregate error across all subjects and dimensions. We applied this analysis multiple times using models generated with a variety of configuration parameters (see Table I for a listing of model generation cases) to identify settings that produced the best results.

Mask Size Prediction

Each subject was fit with at least one of each of the three sizes (Small, Medium, and Large) of the Avon C50. The OSHA standard fit test methodology (OSHA Standards) was followed to produce a fit score by measuring aerosols inside and outside the mask in various postures and various facial expressions. A score of at least 500 was considered passing, and if multiple sizes resulted in a passing score, the highest score was used as the best fit.

To predict mask size, MASQ uses distributions from both a bivariate fit panel, based on face height and face width, and a PCA fit panel (Zhuang, et al., 2008) that takes into account ten different facial measurements. MASQ uses measurements derived from the generated 3D model to identify the cell of each fit panel that the subject falls into. Based on data correlating fit panel cells and respirator size (Zhuang, et al., 2008), each fit panel cell is associated with a percentage of subjects that fit a particular size. MASQ selects the size with the maximum fit percent from both the bivariate and PCA fit panels. It uses the size selected from the PCA panel cell unless the subject did not fit within any cell, in which case it uses the size associated with the bivariate panel cell. In the case that the subject falls below the threshold of both fit panels, size small is predicted, and if the subject falls above the threshold, size large is predicted. While a small number of subjects did fall outside the bounds of the fit panel measurement thresholds, it wasn't specifically recorded as it is just another indication of measurement estimation inaccuracy which is already captured.

To measure accuracy we compared the size predicted by the MASQ algorithm with the size determined by the fit test to produce a percent accuracy, calculated as the number of size matches divided by the number of tests. We measured accuracy multiple times using models generated with a variety of configuration parameters (see Table I for a listing of model generation cases) to identify settings that produced the best results. Since our goal was to replicate the mask size recommendation resulting from the fit-testing process, we did not consider whether MASQ predicted a size that had a passing fit-test score, however this may be worth exploring in the future.

RESULTS

Figure 9 shows the percent error of EOC measurements derived from the scale card image for each subject. The average error was 5.19%, and the median error was 4.00%.

Figure 10 is a plot of the average accuracy of measurement estimates, and the average accuracy of size predictions for all subjects when using measurements derived from eight model generation configurations. The eight cases presented were based on observations of parameters that produced reliable results across all phases of the model generation process and were selected to provide a sampling of possible combinations. Also included are two control cases, the MEAN case, which used the unmodified morphable model for all subjects, and the MEASURED case, which used the hand-measurements instead of estimating measurements from a 3D model. The Measurement Estimate accuracy in Figure 10 is computed by calculating the accuracy of each individual dimension estimate as a percentage of the hand-measurement, then taking the average of all accuracies. The sizing accuracy is computed by calculating the percentage of subjects for which the predicted size matched the size recommended by the subject's fit test. For each model generation case, four configuration parameters were varied:

1. **Model Resolution:** Either the low-resolution or high-resolution SFM
2. **Number of Input Images:** The number of input images used to construct the 3D model
3. **Maximum Pose Angle (MPA):** The maximum allowable deviation from center of a subjects facing angle
4. **Landmarks Detected:** Either the 68 or 103 landmark detection model

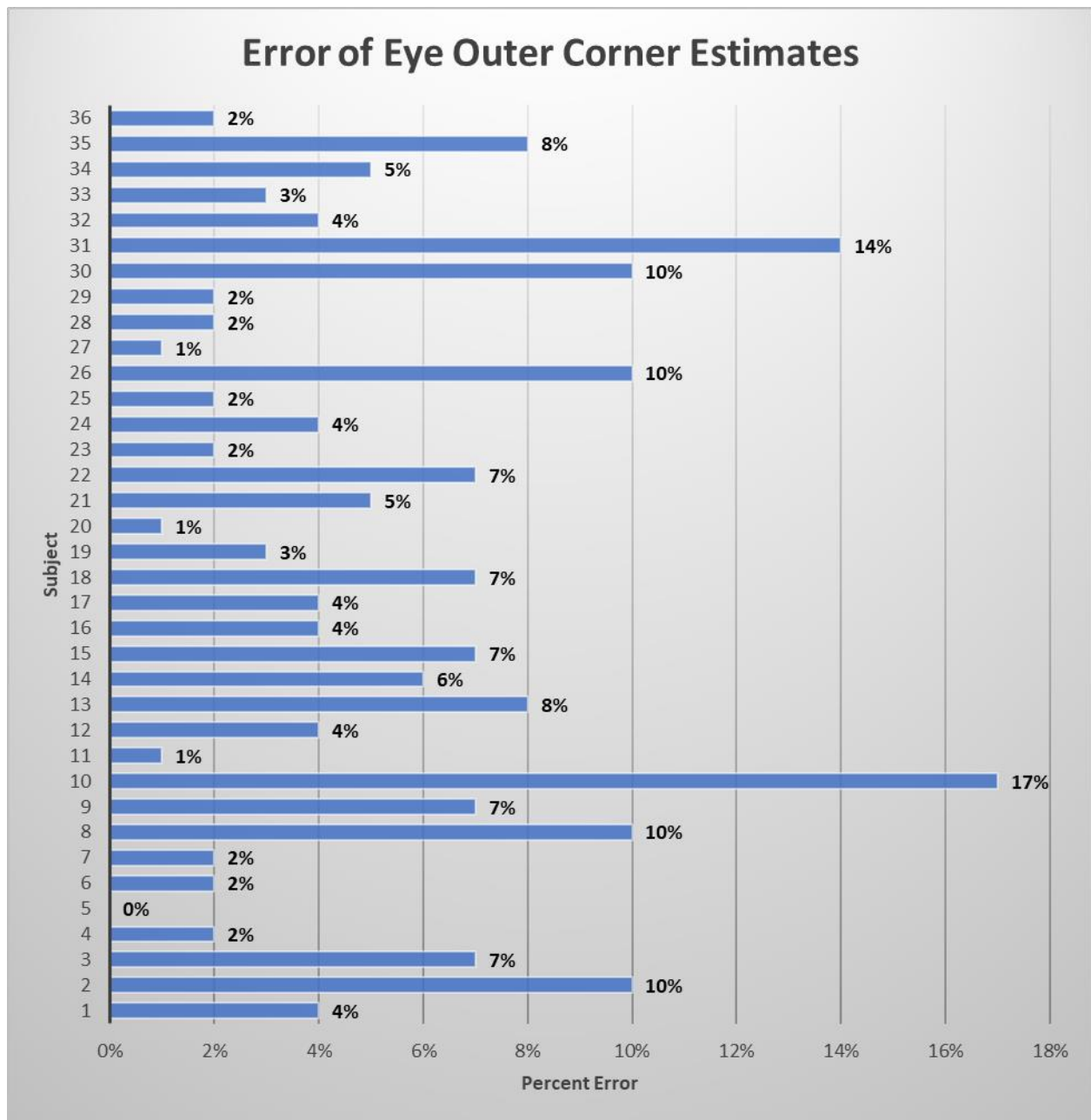


Figure 9. EOC estimate errors relative to hand-measured values for each subject.

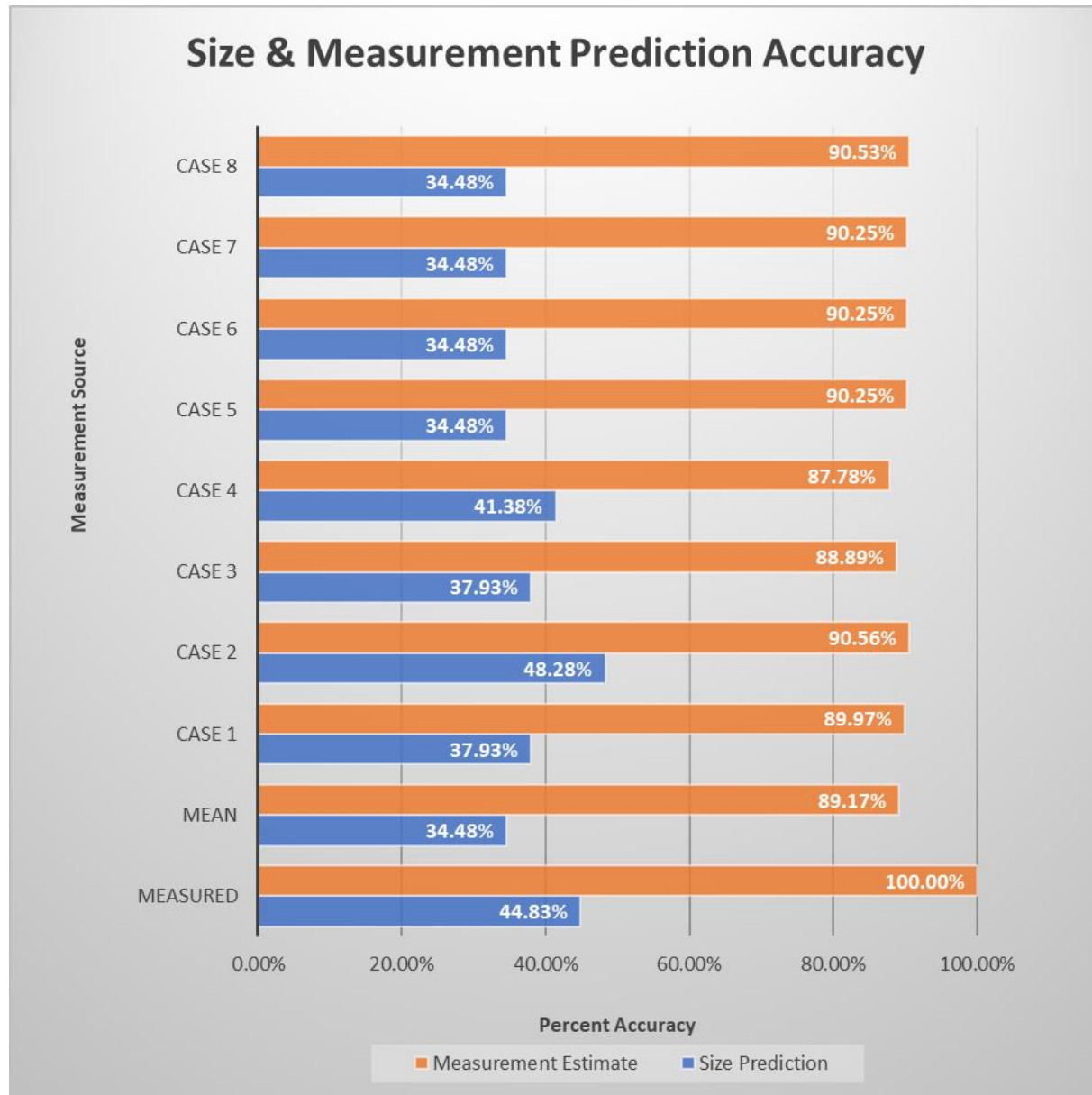


Figure 10. Average percent accuracy of measurement estimates and size predictions across all subjects for eight different model generation cases and two control cases.

Table II describes the specific model generation parameters used for cases 1 through 8.

Table II. Descriptions of Test Cases (each case includes the resolution of the model used, the number of images used to generate the model, the max. pose angle for input images, and the number of landmarks detected for each image)

Measurement Source	Model Resolution	# Input Images	Max.Pose Angle	Landmarks Detected
CASE 1	Hi-res	1	n/a	68
CASE 2	Low-res	1	n/a	68
CASE 3	Low-res	1	n/a	103
CASE 4	Low-res	12	+/- 10 degrees	103
CASE 5	Low-res	20	+/- 5 degrees	68
CASE 6	Low-res	20	+/- 10 degrees	68
CASE 7	Low-res	20	+/- 20 degrees	68
CASE 8	Low-res	100	+/- 20 degrees	68

Sources of Error

Estimated measurement error comes from three primary sources, landmark detection, 3D model morphing, and scale calculation. We have not independently measured landmark detection or orientation accuracy, however it could be done by manually annotating images with landmarks as the source of ground truth and comparing with the automatically detected locations. Similarly, 3D model morphing has not been independently measured, and doing so is more difficult as it would require a source of ground truth for landmarks in 3D space, such as a high resolution scan. Scaling card accuracy is presented in Figure 8, with error being introduced from automated detection of the EOC landmarks, placement of the scaling card either in front of or behind the line connecting EOC landmarks, orientation of the scaling card that is not parallel to the camera, and measurement of the height and width in pixels of the black square on the scaling card within the image.

CONCLUSIONS

Conclusions of the Verification and Validation

From the V&V study, we found that size prediction using the best-case scenario of hand-measured facial dimensions produced an accuracy rate of 45%. This result indicates a shortcoming of the size prediction methodology and that using fit-panel correlation does not produce sufficiently accurate predictions to replace fit-tests.

However, model generation case 2 (see figure 9) produced the most accurate size predictions (48%), even performing better than the hand-measured case. While better performance than hand-measured values is likely an anomaly, it does indicate that predicting size via model generation can perform just as well as hand-measurement. This result indicates that if an algorithm that predicts mask sizes given hand-measured dimensions can be developed, then MASQ model generation could be a viable replacement for the time and resource intensive hand-measurement process.

Also of note is that case 2 performed better than cases that used more images for model generation. Although the goal of additional images is to refine the model to better conform to the subject's face, it in fact seems to introduce error. Initial tests show that as the pose angle increases, the probability

that landmarks that are inaccurately detected increases. While filtering out images beyond the MPA threshold aims to mitigate this issue, it can be unreliable because it relies on computing the pose angle after landmarks have been detected. In many cases, even when a face is beyond the MPA threshold, the model erroneously detects landmarks that do fall within the MPA threshold, merging them into the final model and reducing accuracy.

MASQ Application

MASQ is an easy to use mobile app for generating customized 3D head forms for individuals, estimating facial measurements, and predicting respirator size. While size prediction is still lacking, MASQ offers additional features not described in this paper that make it a useful tool for individuals, as well as researchers. MASQ supports multi-user operation and online data storage, making it a useful tool for conducting studies and collecting measurement and model data. For individuals, it features a tool to analyze hairlines and detect potential interference with mask seals, and it includes a guided training workflow to ensure users not only use a properly sized mask, but also understand how to properly inspect, don, and tighten their protective equipment. MASQ currently operates on the Android and iOS platforms, however it is not yet generally available.

Future Work

The data collected as part of the MASQ V&V can provide a useful resource for further investigation and model development. By pairing multi-angle images with facial measurements, the V&V data set contains useful information that has previously been unavailable, enabling insights that are not possible with simple linear measurements alone. To make use of these data, we suggest further research to find correlations between facial data and fit-test results. Specifically, we believe a machine-learning approach that is based on multiple dimensions of facial data, including linear measurements, contours, images, and 3D models is likely to provide the most benefit. Although the data collected for this V&V effort are a good start, a successful machine-learning model will likely require more data points, so we suggest a follow-on data collection effort with the goal of collecting measurements, videos, and fit-tests for an additional 100 to 200 subjects. After training and validating a model with the enhanced data set, it could then replace the existing fit-panel-based prediction algorithm while still using MASQ's existing dimensional analysis and 3D model generation capabilities to provide the model inputs.

Another area of future improvement is the scale calculation. Although the scaling card method is accurate in the ideal situation, it is prone to user error, particularly if the card is held significantly in front of or behind the eyes, or held at a severe angle. It can also be cumbersome, and requires printing the image. One option to investigate is the use of technologies integrated into the latest smart phones for the purposes of augmented reality (AR). Apple's ARKit application programming interface (API) supports methods for measuring objects by tracking relative motion in camera frames over time. A combination of landmark detection combined with these measurement capabilities could provide a scale calculation that is both accurate, automatic, and requires no user intervention.

The Avon C50 was selected as the first mask to investigate as it is a commonly used military respirator and was selected by the project sponsor. Exploring fit prediction for masks that are commonly used by the civilian population, such as the N95, is another avenue of future research. MASQ could be adapted to any mask which depends on proper size selection for optimal effectiveness, however, further data collection that pairs facial dimension measurements with proper sizing is first required.

Acknowledgements

The research and development described in this paper was funded by SBIR grants sponsored by the Chemical and Biological Defense program of the U.S. Department of Defense. The V&V data

collection was performed by Anthrotech Inc. and masks used for subject fit testing were supplied by Avon Protection.

REFERENCES

- Biagiotti, E., Korna, M., Rice, D. O., & Barker, D. (2019). Predicting respirator size and fit from 2D images. *International Journal of Human Factors Modelling and Simulation*.
- Canny, J. (1986). A Computational Approach to Edge Detection. *IEEE Trans. on Pattern Analysis and Machine Intelligence*, 8(6), 679-698.
- Clauser, C., Tebbetts, I., Bradtmiller, B., McConville, J., & Gordan, C. C. (1987-1988). *Measurer's Handbook: U.S. Army Anthropometric Survey*. Natick, Massachusetts: United States Army Research, Development, and Engineering Center.
- Huber, P. (2016). *A lightweight 3D Morphable Face Model fitting library in modern C++*. Retrieved from <https://github.com/patrikhuber/eos>
- Huber, P. (2017). *C++ implementation of the supervised descent optimisation method*. Retrieved from <https://github.com/patrikhuber/superviseddescent>
- Huber, P., Feng, Z., Christmas, W., Kittler, J., & Rätsch, M. (2015). Fitting 3D Morphable Models using Local Features. *IEEE International Conference on Image Processing (ICIP)*. Quebec City.
- Huber, P., Guosheng, H., Tena, R., Mortazavaian, P., Koppen, W. P., Christmas, W., . . . Kittler, J. (2016). A Multiresolution 3D Morphable Face Model and Fitting Framework. *The 11th International Joint Conference on Computer Vision, Imaging and Computer Graphics Theory and Applications*. Rome.
- (2015). *ISO/TS 16976-2*.
- Le, V. (2017, December 27). *Helen Dataset*. Retrieved from <http://www.ifp.illinois.edu/~vuongle2/helen/>
- Matas, J., Galambos, C., & Kittler, J. (2000). Robust Detection of Lines Using the Progressive Probabilistic Hough Transform. *Computer Vision and Image Understanding*, 119-137.
- OpenCV Team. (n.d.). *OpenCV Library*. Retrieved 2017, from <https://opencv.org/>
- OSHA Standards. (n.d.). *Appendix A to § 1910.134: Fit Testing Procedures*. Retrieved from Occupational Safety and Health Administration: https://www.osha.gov/pls/oshaweb/owadisp.show_document?p_id=9780&p_table=STANDARDS
- Sagonas, C., Tzimiropoulos, G., Zafeiriou, S., & Pantic, M. (2013). 300 Faces in-the-Wild Challenge: The first facial landmark localization Challenge. *IEEE Int'l Conf. on Computer Vision (ICCV-W)*. Sydney.
- Zhuang, Z., & Bradtmiller, B. (2005). Head-and-face anthropometric survey of U.S. respirator users. *Journal of Occupational and Environmental Hygiene*, 567-576.
- Zhuang, Z., Bradtmiller, B., & Shaffer, R. E. (2007). New Respirator Fit Test Panels Representing the Current U.S. Civilian Workforce. *Journal of Occupational and Environmental Hygiene*, 647-659.
- Zhuang, Z., Groce, D., Ahler, H. W., Iskander, W., Landsittel, D., Guffey, S., . . . Shaffer, R. E. (2008). Correlation Between Respirator Fit and Respirator Fit Test Panel Cells by Respirator Size. *Journal of Occupational and Environmental Hygiene*, 617-628.
- Zhuang, Z., Slice, D. E., Benson, S., Lynch, S., & Viscusi, D. J. (2010). Shape Analysis of 3D Head Scan Data for U.S. Respirator Users. *EURASIP Journal on Advances in Signal Processing*, 2010: 248954.

The Effect of Particle Size, Membrane Type, and Face Velocity on TiO₂-Containing Paint Dust Filtration

Adam W. Nored¹, Marie-Cecile G. Chalbot^{2,3}, Jin Y. Shin⁴ and Ilias G. Kavouras^{2,5}

¹ Interdisciplinary Engineering Program, School of Engineering, University of Alabama at Birmingham, Birmingham, 1075 13th St S, Birmingham, AL 35205, USA

² Department of Environmental Health Sciences, Ryals School of Public Health, University of Alabama at Birmingham, 1665 University Blvd, Birmingham, AL 35233, USA

³ Department of Biological Sciences, School of Arts and Sciences, New York City College of Technology, 300 Jay St, Brooklyn, NY 11201, USA

⁴ Department of Chemical and Environmental Sciences, School of Science, Health and Technology, CUNY Medgar Evers College 1638 Bedford Ave., Brooklyn, NY, 11225, USA

⁵ Department of Environmental, Occupational and Geospatial Health Sciences, CUNY Graduate School of Public Health and Health Policy, 55 W 125th Street, New York, NY 10024, USA

* Corresponding author and E-mail: Ilias.Kavouras@sph.cuny.edu

ABSTRACT

The U.S. Centers of Diseases Control suggests the use filtering facepiece respirators (FFRs) for painters and related construction occupations. Engineered titanium dioxide (TiO₂) nanoparticles, shown to be more tumorigenic than bulk TiO₂, are prevalent in paint formulations. Specific occupational protection protocols are developed to manage tasks associated with TiO₂-containing paints and dust. In this study, the efficacy of different types of filtration membranes, namely, packed polypropylene (used in N95 FFRs), cellulose acetate, polycarbonate and polytetrafluoroethylene to remove paint dust containing TiO₂ nanoparticles was examined at various conditions. The particle mass size distribution of paint dust was measured using real-time 10-stage Quartz Crystal Microbalance (QCM) cascade impactor. Particles above 300 nm were more efficiently removed by cellulose acetate and polytetrafluoroethylene membranes. The filtration efficiency dropped rapidly for smaller particles in the 100-300 nm range. The results showed that the filtration efficiency of packed polypropylene membrane increased as particle size decreased with the highest computed for particles below 100 nm. This may be due diffusion by Brownian motion and electrostatic attraction. The low collection efficiency of cellulose acetate for the most penetrating and harmful particles below 100 nm was improved by increasing the face velocity. These results can be used by manufacturers to select materials for their respirators. The results can also facilitate future studies on the design and optimization of respirators using polypropylene or cellulose acetate membranes to remove the most potent TiO₂-containing ultrafine paint dust particles.

Keywords: Engineered TiO₂ nanoparticles, paint dust, ultrafine particles, N95 membrane, cellulose acetate

INTRODUCTION

Since 1973, occupational and environmental protections agencies such as CDC, Occupational Safety and Health Administration (OSHA) and US Environmental Protection Agency (EPA) have been dealing with Pb-based paints consequences. Yet, an equally harmful and detrimental public health emergency may be brewing due to nanoparticles (NPs) containing paints (Muller *et al* 2018). TiO₂ is the most used white pigment in paints (ca. 70% of the total pigments) because of its high stability, anticorrosive and antibacterial properties. TiO₂ exists in different particle size fractions as fine particles (FPs) (diameter 0.1-2.5 µm) and nanoparticles (NPs) (diameter < 0.1 µm or 100 nm) (Ortlieb *et al* 2010). TiO₂ NPs embedded into paint may be less harmful because of agglomerate formation; however, the NPs are released upon degradation during weathering and sanding. The major exposure route of TiO₂ NP is inhalation in occupational settings. Sanding dust coated with nanoparticle containing paint was shown to be dominated by nano size particles (<300 nm) containing up to 80% TiO₂ and other NPs (Koponen *et al* 2015; Nored *et al* 2018).

Upon entry into the human body, TiO₂ NPs are absorbed and translocated across the air-blood barrier, distributed to organs and tissues by systemic circulation and interact with plasma-proteins, coagulation factors, platelets, and blood cells (Geiser *et al* 2010; Lee *et al* 2011; Eydner *et al* 2012). *In vivo* studies demonstrated the carcinogenic potential of TiO₂ NPs, with TiO₂ NPs being more tumorigenic than TiO₂ FPs on an equal mass dose basis (Trochimowicz *et al* 1988; Heinrich *et al* 1995). Owing to their relatively short time in use, early epidemiological studies did not detect an association between occupational exposure to TiO₂ particles and an increased lung cancer risk (Fryzek *et al* 2003). Moreover, the association of TiO₂ particle size, the most important determinant of TiO₂ NPs carcinogenicity, with lung cancer risk is not well studied. It is estimated that lifetime occupational exposures of TiO₂ NPs from 70 µg/m³ to 700 µg/m³ are associated with 0.1% excess risk of lung cancer (Dankovic *et al* 2007). Exposure and dose-response analysis across the lifecycle of products is seriously lacking for both occupational and environmental scenarios particularly in relation to particle size and processes generating high TiO₂ NP concentrations. It is, therefore, appropriate to control and mitigate TiO₂ NP exposures to reduce the burden on occupational health and safety, particularly for painters who already have a high prevalence of lung diseases, such as cancer (Lim *et al.*, 2012), and chronic obstructive pulmonary disease (COPD) (Wang *et al.*, 2016). Paint dust emissions are the ninth leading cause of disease in the coatings industry (Ringén *et al.*, 2014).

The US OSHA recommended an exposure limit for TiO₂ NPs at 0.3 mg/m³ (NIOSH 2011). TiO₂ NPs are also classified by the International Agency for Research of Cancer (IARC) as a Group 2B (possibly carcinogenic to humans) agent suggesting that products containing TiO₂ NPs should be managed cautiously (Baan 2007). Yet, more than 80% of workers and most consumers are not aware about the presence of NPs in paints (West *et al* 2016). Personal protective equipment such as N95 FFRs (i.e., removing at least 95% of particles 0.3 µm (or 300 nm) mass median aerodynamic diameter) have demonstrated poorer filtration of particles in 20-100 nm size range (may exceed 5%) with the most penetrating particle size at approximately 50 nanometers (Eninger *et al* 2008). Pre-charged fiber filters have the poorest protection from particles between 35-70 nanometers (Balazy *et al* 2005).

The goal of the study was to assess the efficiency of filtration membranes used for respiratory protection including polypropylene in N95 FFRs (i.e., designed to remove at least 95% of all airborne particles) to remove ultrafine paint dust particles containing engineered TiO₂ nanoparticles. In addition, the effects of particle size and face velocity was examined. Large porosity polycarbonate membrane was used to validate the role of porosity of particle filtration. Realistic TiO₂-containing paint dust was generated using a previously developed experimental apparatus (Nored *et al* 2017). Organic-based paint agglomerates included titanium dioxide NPs predominantly for particles with sizes < 100 nm. This was consistent with previous studies showing the accumulation of engineered NPs in ultrafine paint dust (Koponen *et al* 2011).

MATERIALS AND METHODS

Materials

A commercially available latex paint and primer formulation for indoor surfaces was used to coat wood panels. It was composed of water (49.6% w/w), non-volatile species (49.4% w/w), organic volatiles (0.9% w/w) and 2-amino-2-methyl-1-propanol (0.2% w/w) (CAS #: 124-68-5), TiO₂ (3.2% w/w) (CAS #: 13463-67-7), crystalline silica (0.22% w/w) (CAS #: 14808-60-7) and cristobalite (0.11% w/w) (CAS #: 14464-46-1). For abrasion, a BDERO600 2.4 Amp 5 inches (12.7 cm) orbital sander in its complete configuration (including the fitted filter) (Black & Decker, Towson, MD) fitted with Shopsmith® 5 inches (12.7 cm) aluminum oxide abrasive film discs with 120 grit (Shopsmith, Dayton, OH). The four membranes chosen were cellulose acetate (0.2 µm pore size, 47-mm, Pall, MI), polytetrafluoroethylene (PTFE) (2.0 µm, pore size, 47-mm, SKC Inc, PA), polycarbonate (Nuclepore®) (8 µm, pore size, 47-mm, Corning, NY) and polypropylene (N95, 3M 8210, St. Paul, MN).

Paint Dust Generation and Measurement

The Coatings Aerosol Resuspension System (CARES) was used to generate TiO₂ containing paint dust (Figure 1; Nored *et al* 2017). Briefly, paint dust polydisperse particles were generated from manually coated wood panels using an orbital sander in a polyvinylchloride glove box chamber (115 cm x 60 cm x 60cm) (Lancs Industries, Kirkland, WA). The efficiency of four membranes to collect TiO₂-containing paint dust was assessed by monitoring the size distribution of generated paint dust in the CARES (i.e., upstream) and after the membrane (i.e., downstream) for 5 min, simultaneously, and repeated at least six times (using a new wood panel each time) in order to get reproducible and accurate measurements. The collection efficiency of the four membranes was tested at face velocity of 1.92 cm/s. In addition, the collection efficiency of cellulose acetate membrane was measured at flow rates (Q: from 2 to 6 L/min) corresponding to face velocity of 1.92 to 5.76 cm/s and Reynolds number (Re) from 60 to 180.

The real-time 10-stage Quartz Crystal Microbalance (QCM) cascade impactor system (Model PC-2H, California, US) was used to measure particle mass in ten stages with 50% cut-off aerodynamic diameter cut-off points of 14, 9.7, 4.2, 2.8, 1.4, 0.7, 0.45, 0.30, 0.16 and 0.10 µm at 2 L/min flow rate. The average sensitivity is 1.4 ng per Hz but varies for each impactor stage because of differences in particle deposition in each stage. For typical ambient conditions, the signal-to-noise (S/N) ratio was more than 20, sufficient to adequately measure particle mass without crystal overloading. The impaction substrates (i.e., sensing crystals) were cleaned between experiments with n-hexane, and re-calibrated per manufacturer's protocol. In addition, the agreement between the two instruments was also assessed at the beginning and end of each experiment using indoor air for 15-20 minutes.

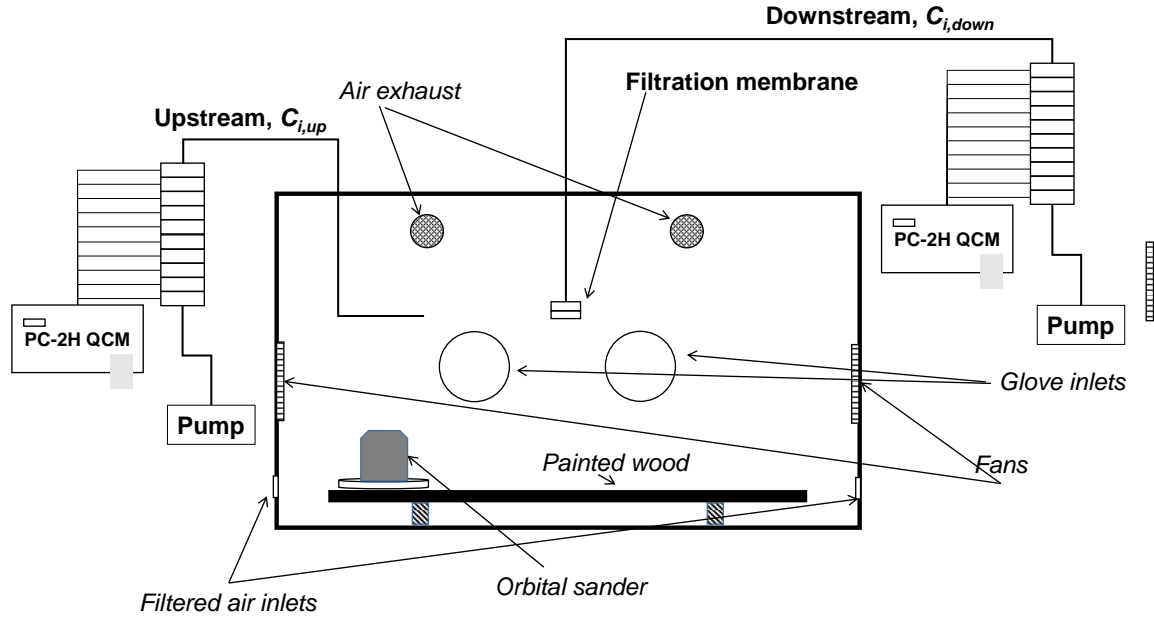


Figure 1. Schematic diagram of the experimental apparatus. Paint dust is generated into the chamber. The generated aerosol is measured in the chamber (Upstream, $C_{i,up}$) and after the filtration membrane (Downstream, $C_{i,down}$).

Total and size-dependent collection efficiency

The total (E_t) and size-dependent (E_i) collection efficiencies (dimensionless) were calculated using downstream ($C_{i,down}$) and upstream ($C_{i,up}$) particle mass concentrations as follows:

$$E_t = 1 - \frac{\sum_{i=1}^{10} C_{i,down}}{\sum_{i=1}^{10} C_{i,up}} \quad (1)$$

and

$$E_i = 1 - \frac{C_{i,down}}{C_{i,up}} \quad (2)$$

Statistical analysis

Particle mass concentrations were tested for normality using the Shapiro-Wilk test. The significance of difference in mean particle mass concentration values between groups was examined with the non-parametric Mann-Whitney (when two groups were compared) and Kruskal-Wallis (for more than two groups) tests at $\alpha=0.05$. These tests were followed by Tukey's Honestly Significant Difference test. All analyses were done using SPSS (Version 25) (IBM Analytics, Armonk, NY) and Origin Pro (version 9.1) (OriginLab, Northampton, MA).

RESULTS

Figure 2 shows the representative relative size distribution of TiO_2 -containing paint dust mass concentration in the CARES system (upstream) and after the cellulose acetate membrane (downstream). The total particle mass concentration was $540 \pm 60 \mu\text{g}/\text{m}^3$ for upstream and $17 \pm 1 \mu\text{g}/\text{m}^3$ for downstream ($p < 0.001$). The upstream concentration was comparable to that computed for paint dust using the same experimental configuration as previously ($864 \pm 503 \mu\text{g}/\text{m}^3$; Nored *et al* 2018). Particles in the accumulation mode range (100 nm – 1.4 μm) accounted for most of the upstream paint dust mass (ca. 61%) but less than 35% of downstream paint dust mass. Note that particles with diameter < 100 nm account for a small fraction of particles by mass but their particle number concentration is 2-3 orders of magnitude higher than particles with diameter < 1 μm (Nored *et al* 2018).

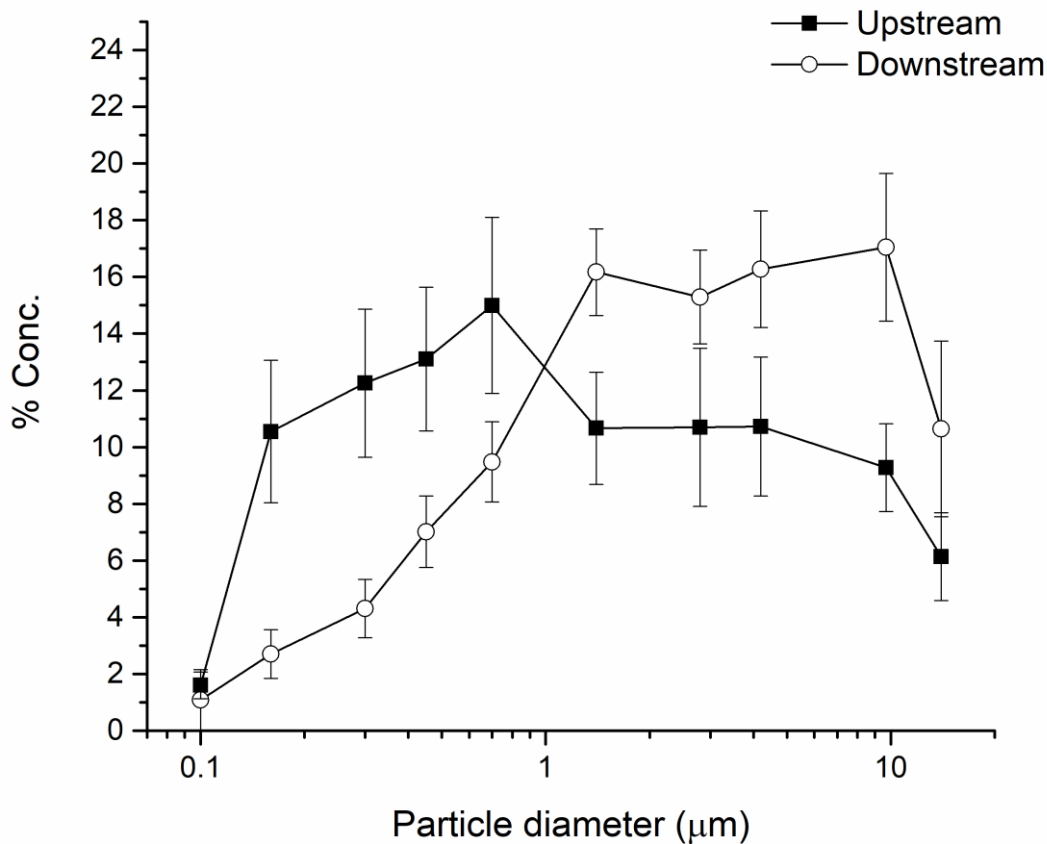


Figure 2. Percent relative mass (to the total particle mass) concentration of polydisperse paint dust aerosol upstream and downstream of cellulose acetate membrane at a face velocity of 1.92 cm/s in the CARES system. Squares and circles represent the average of at least six replicates of upstream and downstream concentration measured simultaneously. Error bars corresponds to $1.96 \times$ standard error.

The collection efficiencies (E_t , dimensionless) as a function of particle size of each membrane at face velocity of 1.92 cm/s are shown in Figure 3. We compared polypropylene (the filter medium used for the NIOSH-recommended N95 FFRs), PTFE, and cellulose acetate membranes that are typically used for the collection of atmospheric aerosols. In addition, we also measured the collection efficiency of a porous polycarbonate membrane (pore size 8 μm). The polycarbonate membrane showed the poorest collection efficiency allowing for the penetration of most of the particles in the 0.45 – 9.7 μm size range (efficiencies varied from 11.6 % to 75%) due to its large pore size. Cellulose acetate and PTFE membranes filtered above 300 nm particles with efficiencies > 99% and rapidly declined for smaller particle sizes. In comparison, the filtration efficiency of N95 polypropylene membrane increased as particle size decreased with the highest efficiencies (i.e., 96-99%) computed for particles below 150 nm. Particles above 10 μm were less efficiently collected (90-95%) by all membranes.

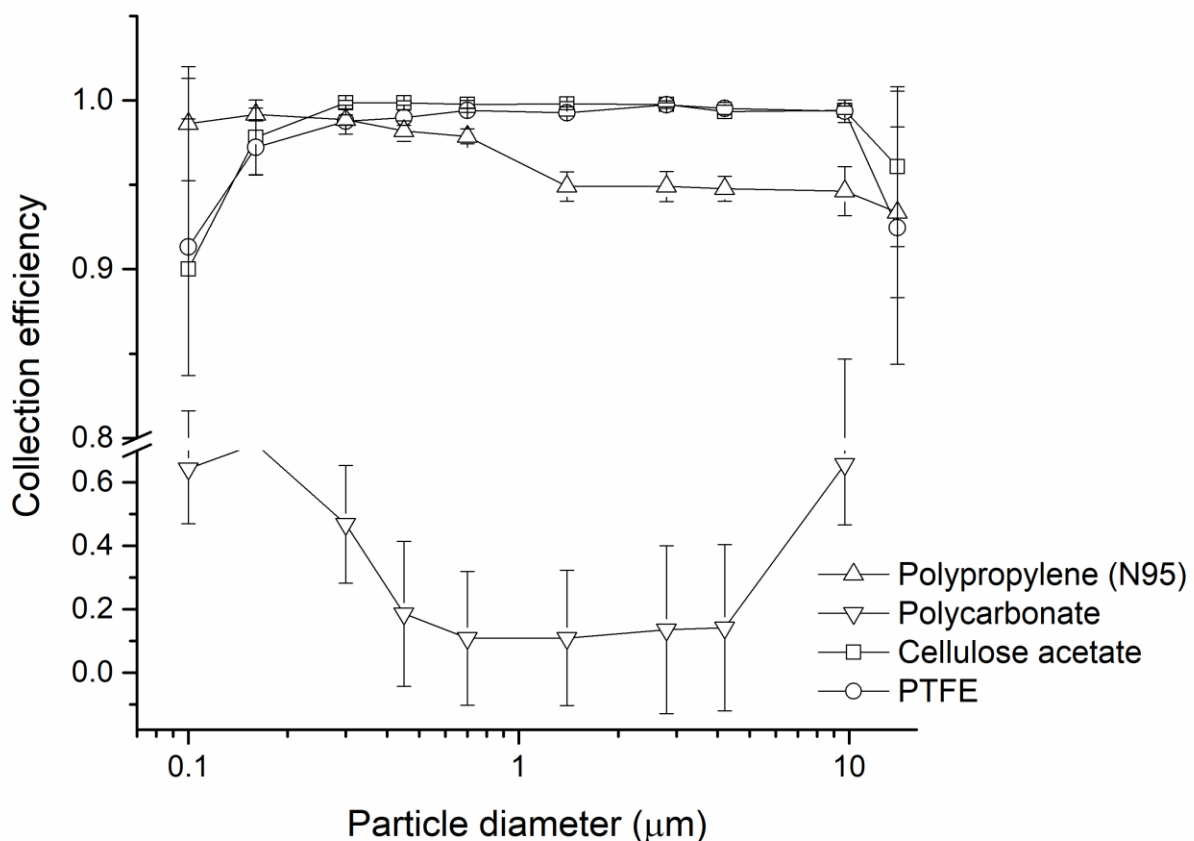


Figure 3. Collection efficiencies of polydisperse paint dust aerosol upstream and downstream of various membranes at a face velocity of 1.92 cm/s in the CARES system. Squares, circles, and triangles represent the average of at least six replicates of upstream and downstream concentration measured simultaneously. Error bars corresponds to $1.96 \times$ standard error.

Table I summarizes the key findings of the efficiencies for all particles (E_t), and particles with diameter < 300 ($E_{<300}$) and < 100 ($E_{<100}$) nm of the membranes at different face velocities. Polypropylene membrane performed as designed to collect more than 95% of the particles above 300 nm ($96.8\% \pm 18.8\%$), but also particles below 300 nm ($98.9\% \pm 4.2\%$). The collection efficiencies of both cellulose acetate and PTFE membranes were superior (more than 99%) to that of polypropylene membranes for particles above and below 300 nm. However, the collection efficiencies for particles below 100 nm of cellulose acetate and PTFE membranes dropped to approximately 90% as compared to about 99% for polypropylene membranes.

Higher face velocities (3.84 and 5.76 cm/s) did not change the already high filtration efficiencies of particles above 300 nm but increased the filtration efficiency of particles below 100 nm up to $96.8\% \pm 18.8\%$ at 3.84 cm/s and $96.8\% \pm 18.8\%$ at 5.76 cm/s (Figure 4). Despite the increase, the other membranes were still inferior to the polypropylene membrane for the filtration of particles below 100 nm.

Table I. Filtration Efficiencies of Various Membranes at Flow Rates of 2, 4 and 6 L/min

<i>Filter material</i>	<i>Pore size</i>	<i>Q (L/min)</i>	<i>U (cm/sec)</i>	<i>% E_t</i>	<i>% $E_{<300}$</i>	<i>% $E_{<100}$</i>
Polypropylene (N95)	n/a	2.0	1.92	96.8 ± 18.8	98.9 ± 4.2	98.6 ± 1.2
Polycarbonate	8 μm	2.0	1.92	11.6 ± 38.3	64.1 ± 26.8	64.3 ± 8.2
Polytetrafluoroethylene	2 μm	2.0	1.92	99.5 ± 12.4	99.6 ± 8.4	91.3 ± 3.2
Cellulose acetate	0.2 μm	2.0	1.92	99.7 ± 16.0	99.6 ± 13.1	90.0 ± 4.7
Cellulose acetate	0.2 μm	4.0	3.84	99.1 ± 10.7	99.1 ± 5.3	93.6 ± 1.9
Cellulose acetate	0.2 μm	6.0	5.76	99.5 ± 1.6	99.2 ± 1.0	95.8 ± 3.6

DISCUSSION

Commercially available personal protective equipment (PPE), including N95 FFRs, are intended to efficiently remove airborne particles. The efficiency of the PPE depends on filtration variables such as face velocity, particle size, membrane material and porosity as well as the use-specific variables including proper fitting (i.e., the gap size between facial profiles and the PPE). Here, we examined the role of filtration variables on the efficiencies of various membranes to remove polydisperse particles of paint-dust, specifically those containing TiO_2 at < 100 nm (Nored *et al* 2018).

It has been shown that total filtration efficiency for particles above 600 nm was high for small pore-size, non-absorbent, hydrophobic thermoplastic polymer-based membranes (Akalin *et al* 2010). Inertial impaction and gravitation sedimentation may be the dominant mechanism for particles above 1 μm . The filtration efficiency for particles above 1 μm increased as face velocities increased, due to higher inertia. As particle size decreased from 1 μm to 100 nm, Brownian diffusion, and mechanical interception of particles by the filter fibers were the prevailing filtration mechanisms. Improved filtration efficiency may also be attributed to electrostatic attraction. The surface of TiO_2 NPs is found to be positive at pH less than 6.0 (Ramirez *et al* 2019) as compared to negatively charged PTFE and cellulose acetate (CH_3COO^-) membranes (He *et al* 2020). Polypropylene membranes are also considered electrostatic filters.

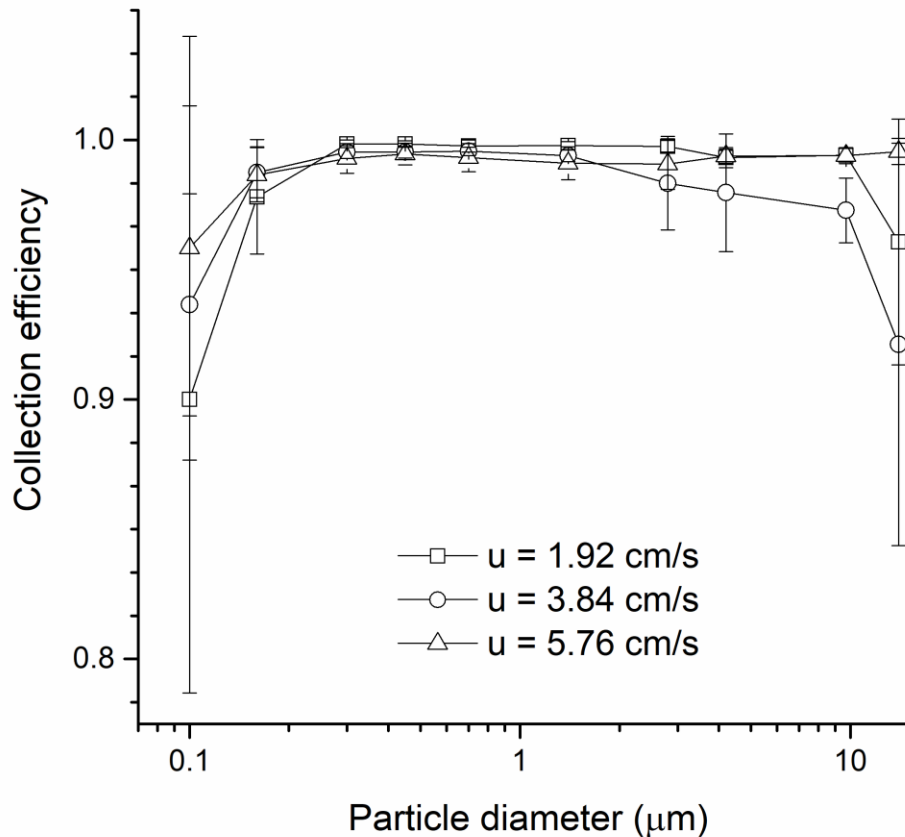


Figure 4. Collection efficiencies of polydisperse paint dust aerosol upstream and downstream of cellulose acetate at a face velocities of 1.92, 3.84 and 5.76 cm/s in the CARES system. Squares, circles, and triangles represent the average of at least six replicates of upstream and downstream concentration measured simultaneously. Error bars corresponds to $1.96 \times$ standard error.

The filtration efficiency of particles below 300 nm was higher for PTFE and cellulose acetate than polypropylene membrane. The opposite was true for particles below 100 nm; the filtration efficiency of polypropylene membrane was higher than PTFE and cellulose acetate. This observation may be attributed to packing density, thickness, or fiber charge density in N95 FFRs polypropylene membranes as compared to thinner PTFE and cellulose acetate membranes (Huang *et al* 2013). It is noteworthy that diffusion and electrostatic attraction, the dominant mechanisms for the filtration of particles below 100 nm, differ for various conditions including face velocity and particle size, particularly in the nano-size range. For example, the electrostatic attraction is less effective as face velocity increases because of lower residence time (Givchchi *et al* 2015). The thermal rebound effect, i.e., the likelihood of particle detachment due to high thermal velocity and kinetic energy may further reduce the collection of particles below 100 nm at higher velocities. On the other hand, surface adhesion and elasticity, and the surface coating and potential to aggregate may limit thermal rebound and increase filtration efficiency for particles

below 100 nm (Warheit *et al* 2008). In addition, the filtration of particles below 100 nm increase over time due to filter loading. It has been shown that the capture of particles below 100 nm increases with increasing the loading time through the formation of dendrite crystals on single fibers (Bahloul *et al* 2014).

CONCLUSIONS

We have measured the filtration efficiencies of various commonly used membranes to filter paint dust particles containing TiO₂ NPs in the physiologically hazardous ~10 nm to 300 nm size range. We found that cellulose acetate and PTFE membranes efficiently filtered more than 99% of particles above 300 nm by mass, however their efficiency declined for particles below 100 nm. On the other hand, packed polypropylene membranes obtained from N95 masks showed filtration efficiencies slightly above 95% for particles above 300 nm, and higher filtration efficiency for particles below 300 and 100 nm. This may be attributed to the increased particle filtration by diffusion and electrostatic attraction in packed polypropylene membranes. The increase of the filtration efficiency of particles below 100 nm for PTFE and cellulose acetate membranes for higher face velocities may be due to the loading effect of previously collected particles in high concentration paint dust conditions.

REFERENCES

- Akalin, M.; Usta, I.; Kocak, D.; Ozen, M.; (2010) Investigation of the filtration properties of medical masks. *Medical and Healthcare Textiles* 93-97.
- Baan, R.A., (2008) Carcinogenic hazards from inhaled carbon black, titanium dioxide, and talc not containing asbestos or asbestiform fibers: recent evaluations by an IARC Monographs Working Group. *Inhalation Toxicology* 2007;19 Suppl 1:213-228.
- Bahloul, A.; Mahdavi, A.; Haghighat, F.; Ostiguy, C., (2014) Evaluation of N95 filtering facepiece respirator efficiency with cyclic and constant flows. *Journal of Occupational and Environmental Hygiene* 11(8):499-508.
- Balazy, A.; Toivola, M.; Reponen, T.; Podgórski, A.; Zimmer, A.; Grinshpun, S.A., (2005) Manikin-based performance evaluation of N95 filtering-facepiece respirators challenged with nanoparticles. *Annals of Occupational Hygiene* 50, 259–269.
- Dankovic, D.; Kuempel, E.; Wheeler, M., (2007). An approach to risk assessment for TiO₂. *Inhalation Toxicology* 19, 205-212.
- Eninger, R.M.; Honda, T.; Adhikari, A.; Heinonen-Tanski, H.; Reponen, T.; Grinshpun, S.A., (2008) Filter Performance of N99 and N95 Facepiece Respirators Against Viruses and Ultrafine Particles. *Annals of Occupational Hygiene* 52, 385–396.
- Eydner, M.; Schaudien, D.; Creutzenberg, O.; Ernst, H.; Hansen, T.; Baumgärtner, W.; Rittinghausen, S., (2012) Impacts after inhalation of nano- and fine-sized titanium dioxide particles: morphological changes, translocation within the rat lung, and evaluation of particle deposition using the relative deposition index. *Inhalation Toxicology*, 24:9, 557-569, DOI: [10.3109/08958378.2012.697494](https://doi.org/10.3109/08958378.2012.697494)
- Fryzek, J.P.; Chadda, B.; Marano, D.; White, K.; Schweitzer, S.; McLaughlin, J.K.; Blot, W.J., (2003) A cohort mortality study among titanium dioxide manufacturing workers in the United States. *Journal of Occupational and Environmental Medicine* 45(4):400-409.
- Geiser, M.; Kreyling, W.G., (2010) Deposition and biokinetics of inhaled nanoparticles. *Particle Fibre Toxicology* 7, 2. <https://doi.org/10.1186/1743-8977-7-2>
- Givhchi, R.; Li, Q.; Tan, T., (2015) The effect of electrostatic forces on filtration efficiency of granular filters. *Powder Technology* 277, 135-140.
- He, W.; Zhao, Y.-B.; Jiang, F.; Guo, Y.; Gao, H.; Liu, J.; Wang, J., (2020) Filtration performance and charge degradation during particle loading and reusability of charged PTFE needle felt filters. *Separation and Purification Technology*, 233, 116003.

- Heinrich, U.; Fuhst, R.; Rittinghausen, S.; Creutzenberg, O.; Bellmann, B.; Koch, W.; Levsen, K., (1995) Chronic Inhalation Exposure of Wistar Rats and two Different Strains of Mice to Diesel Engine Exhaust, Carbon Black, and Titanium Dioxide, *Inhalation Toxicology*, 7:4, 533-556.
- Huang, S.-H; Chen, C.-W.; Kuo, Y.-M.; Lai, C.-Y.; McKay, R.; Chen, C.-C., (2013) Factors affecting filter penetration and quality factor of particulate respirators. *Aerosol and Air Quality Research* 13(1), 162-171.
- Koponen, I.M.; Jensen, K.A.; Schneider, T., (2011) Comparison of dust released from sanding conventional and nanoparticle-doped wall and wood coatings. *Journal of Exposure Science and Environmental Epidemiology* 21:408–418.
- Lee, J. H.; Kwon, M.; Ji, J. H.; Kang, C. S.; Ahn, K. H.; Han, J. H.; Yu, I. J., (2011). Exposure assessment of workplaces manufacturing nanosized TiO₂ and silver. *Inhalation Toxicology*, 23(4), 226–236.
- Lim, S.S.; Vos, T.; Flaxman, A.D.; Danaei, G.; Shibuya, K.; Adair-Rohani, H., (2012) A comparative risk assessment of burden of disease and injury attributable to 67 risk factors and risk factor clusters in 21 regions, 1990–2010: a systematic analysis for the Global Burden of Disease Study. *Lancet* 380(9859):2224–2260.
- Muller, C.; Sampson, R.J.; Winter, A.S., (2018) Environmental Inequality: The Social Causes and Consequences of Lead Exposure. *Annual Review of Sociology* 44:1, 263-282.
- NIOSH. Current Intelligence Bulletin 63. Cincinnati: National Institute for Occupational Safety and Health; 2011. Occupational Exposure to Titanium Dioxide.
- Nored, A.W.; Chalbot, M.C.-C.G.; Kavouras, I.G., (2018) Characterization of paint dust aerosol generated from mechanical abrasion of TiO₂-containing paints, *Journal of Occupational and Environmental Hygiene* 15:9, 629-640, DOI: 10.1080/15459624.2018.1484126.
- Ortlieb, M., (2010). White Giant or White Dwarf?: Particle Size Distribution Measurements of TiO₂. *GIT Laboratory Journal Europe*, 14, 42-43.
- Ramirez, L.; Ramseier Gentile, S.; Zimmermann, S.; Stoll, S., (2019) Behavior of TiO₂ and CeO₂ Nanoparticles and Polystyrene Nanoplastics in Bottled Mineral, Drinking and Lake Geneva Waters. Impact of Water Hardness and Natural Organic Matter on Nanoparticle Surface Properties and Aggregation. *Water* 11, 721. <https://doi.org/10.3390/w11040721>
- Ringen, K.; Dement, J.; Welch, L.; Dong, X.S.; Bingham, E.; Quinn, P.S., (2014) Risks of a lifetime in construction. Part II: Chronic occupational diseases. *American Journal of Industrial Medicine* 57(11):1235–45.
- Trochimowicz, H.J.; Lee, K.P.; Reinhardt, C.F., (1988). Chronic inhalation exposure of rats to titanium dioxide dust. *Journal of Applied Toxicology*, 8:383–385.
- Wang, X.; Dong, X.S.; Welch, L.; Largay, J.; (2016) Respiratory Cancer and Non-Malignant Respiratory Disease-Related Mortality among Older Construction Workers-Findings from the Health and Retirement Study. *Occupational and Medical Health Affairs* 4:235.
- Warheit, D.B.; Sayes, C.M.; Reed, K.L.; Swain, K.A., (2008) Health effects related to nanoparticle exposures: environmental, health and safety considerations for assessing hazards and risks. *Pharmacology & Therapeutics* 120(1), 35-42.
- West, G.H.; Lippy, B.E.; Cooper, M.R.; Marsick, D.; Burrelli, L.G.; Griffin, K.N.; Segrave, A.M., (2016) Toward responsible development and effective risk management of nano-enabled products in the U.S. construction industry. *Journal of Nanoparticle Research* 18(2), 1-27.

**ISRP2024****OXFORD****September 22 - 26, 2024**

Pembroke College

oxford.isrp.com

The International Society for Respiratory Protection Biennial Conference 2024

ANNOUNCEMENT

The European Section of the International Society for Respiratory Protection regrets to announce that owing to the uncertainties around resumption of normal business after COVID-19, the Oxford conference will be delayed to 22nd September – 26th September 2024, and will be held as originally planned at Pembroke College, Oxford University, Oxford, United Kingdom.

More details will follow in subsequent communications.

Instructions for Authors

The Journal of the ISRP (JISRP), the official Journal of the International Society for Respiratory Protection, publishes theoretical and applied research in the field of respiratory protection. The *JISRP* publishes technical papers on original work and new analyses of previous research. In addition, the *JISRP* publishes solicited and unsolicited review articles on topics related to respiratory protection, including, but not limited to, program administration, implementation, and training. Papers will be accepted provided they meet these criteria and have not been or will not be published elsewhere, in whole or in part, without the expressed written permission of the Journal. Papers accepted for publication become the copyright of the *JISRP*.

Manuscript Submission

Please submit the manuscript by email to JISRPeditor@ISRP.com. Please send all inquiries and questions on journal business by email or to:

Journal of the ISRP
Attn: Ziqing Zhuang, Ph.D.
105 Eaglebrook Court
Venetia, PA 15367

All manuscripts must be submitted with a cover letter. The cover letter should identify the principal author, to whom correspondence is addressed, and state that the material is original and has not been submitted, accepted, nor published elsewhere. A statement signed by all authors must be enclosed with the cover letter stating that they have contributed substantially to the research, preparation/revision/production of the manuscript, and approve of its submission to the Journal.

All manuscripts must be submitted in English. They must be typed (double spaced) with one-inch (24 mm) margins. A separate page should indicate the title of the paper, the author's name, email and postal addresses, telephone number, and name of the sponsoring institution where the work was performed. All contact information will be published unless an author requests otherwise.

Manuscripts should be between 20 and 30 pages and use a clear, concise writing style. Shorter manuscripts are encouraged. Longer manuscripts that cannot be shortened may be divided into two parts at the editor's discretion. Abstracts should be between 250 and 300 words.

Manuscripts should be organized and presented as follows:

- (a) *Abstract*: Between 250 and 300 words, summarizing the results and conclusions. No acronyms, references, tabular or graphic data are to be included in the abstract. It should include all of the following elements:

Background - What was the main reason for the work?

Objective - What was the goal or intent of the study?

Methods - What essential methods were employed?

Results - What were most significant findings?

Conclusion – What was the single most significant conclusion?

List up to 10 keywords in a series, in descending order of importance, and separated by commas, after the abstract.

- (b) *Introduction*: Address the reason(s) for doing the work.
(c) *Methods*: Include sufficient information to permit repetition of the work.
(d) *Results*: Present data concisely – redundant information in different formats (graphics) is not acceptable.

- (e) *Conclusions*: Deliberation of significance and conclusions – results are not included.
- (f) *Acknowledgments*: Appropriately recognize persons, programs, and financial support.
- (g) *References*: Textual citation follows the bibliographic style. Place each citation at the end of a sentence, by author and year, enclosed in parentheses [e.g., “Our measurement agreed with previous results (Jones, 1989).”] If the author’s name is used as part of a sentence, place the year in parentheses [e.g., “This effect was discussed by Jones *et al.* (1981), who had analyzed data...”]. Place a list of references at the end of the text. List citations alphabetically in the following form: *Journal Articles* ~ surname, initials, (year), title, edition (publisher, city), page number(s); *Technical Reports* ~ surname, initials, (year), title, institution, city, state (or country), publication number.

The following citations are examples of proper form:

American National Standards Institute. (1980) *American National Standard for Respiratory Protection*. American National Standards Institute, Inc., New York, NY. ANSI Z88.2.

Brown WB and Hollander M. (1977) *Statistics--A biomedical introduction*. New York: John Wiley & Sons, 25-27.

Code of Federal Regulations. (1981) *Respiratory protective devices: Tests for permissibility; Fees*. U.S. Government Printing Office, Office of the Federal Register, Washington, DC. Title 30, CFR, Part 11.

Coffey CC, Campbell DL, Myers WR and Zhuang Z. (1998) Comparison of Six Respirator Fit Test Methods with an Actual Measurement of Exposure: Part II--Method Comparison Testing. *Am. Ind. Hyg. Assoc. J.* 59:862-870.

National Institute for Occupational Safety and Health. (1976) *NIOSH Guide to Industrial Respiratory Protection*. DHEW/National Institute for Occupational Safety and Health, Cincinnati, OH. No. 76-189.

Weinstein L, Swartz MN. (1974) Pathogenic Properties of invading microorganisms. In: Sodeman WA Jr, Sodeman WA, eds. *Pathologic physiology: Mechanisms of disease*. Philadelphia: WB Saunders, 457-472.

Papers accepted for publication are subject to a voluntary page charge of \$80 per page. Authors should indicate in their cover letter whether page charges will be paid. Authors who pay page charges will receive 50 reprints. Nonpayment of page charges does not affect the acceptance or rejection of manuscripts.

Optional Open Access

Authors have the option to publish their paper under open access, whereby for a fee their paper will be made freely available online upon publication where any reader can view and download the paper. The open Access fee is \$1000.

If you do not choose the open access option, your paper will be published with the standard subscription- based access.

Manuscript Production and Format Requirements

Manuscripts submitted to the *JISRP* must follow these guidelines in order to start the review process: assemble the material as follows: title, author(s), affiliation(s), abstract, text, acknowledgments (if

any), references, tables, figure caption lists, and figures. Please use SI units, symbols, and abbreviations (Système International d'Unités) as proposed in *Units, Symbols and Abbreviations* (1972), published by the Royal Society of Medicine, 1 Wimpole Street, London W1M 8AE. English units may be included parenthetically.

All mathematical expressions should be typed. Please distinguish between the lowercase letter, *ell* or **l**, and the number, *one* or **1**; and the upper case letter, *oh* or **O**, and the number, *zero* or **0**. Clearly identify all Greek letters.

Request to Authors
















The author should provide the names and contact information (complete physical and email addresses; telephone number) of as many as three potential reviewers in order to facilitate the peer review process. Co-authors or collaborators within the past three years are ineligible. Also excluded from consideration are individuals who have provided advice or critiques of the submitted manuscript. The editor will consider these individuals in the process of assigning referees.

Letters to the Editor



























The "Letters" section is an open forum for readers to comment and question material published in the *JISRP*. Letters will not be reviewed except to exclude obvious errors and to ensure good taste. The Editor reserves the right to edit for length. Anonymous letters will not be published.

Updated 02/2018

ISRP Would Like to Thank the following Corporate Members

<u>European Section</u>			
	Avon Protection		Blücher GmbH
	Cabot		Confined Spaces Training Services
	Defence Science and Technology Laboratory		Design Reality
	Fire Brigades Union		Fire Safe International
	GVS Filter Technology		Honeywell
	JSP Ltd		Molecular
	Paftec		Portwest
	ProQares		TSI Incorporated
	West Midlands Fire Service		

ISRP Would Like to Thank the following Corporate Members

<u>Americas Section</u>			
	3M		Ator Laboratories
	Calgon Carbon Corporation		GENTEX Corporation
	ISEA		Molecular Products Inc.
	North by Honeywell		Occupational Health Dynamics
	Shalon Chemical Industries Ltd		TSI Incorporated
<u>Japan Section</u>			
	3M Japan Ltd		Air Water Safety Service Inc.
	Gastec Corporation		Koken Ltd
	Kuraray Kuraflex Co., Ltd		Midori Anzen Co Ltd
			Sanko Chemical Industries Co. Ltd
	Shigematsu Works		Sibata Scientific Technology Ltd
	Toyo Safety Industrial Co. Ltd		Yamamoto Kogaku Co., Ltd
<u>Australasian Section</u>			
	The S.E.A. Group		
<u>Korea Section</u>			
	3M Korea		DOBU Life Tech
	Since 1994 Measuring the Environment APM ENGINEERING CO., Ltd.		GVS Korea Ltd.
	engineering		TAEWON SIBATA

**Have you checked
out our web page yet?**



<http://www.isrp.com/>